Directionality of Ambient Noise on the Juan de Fuca Plate: Implications for Source Locations of the Primary and Secondary Microseisms

Journal:	*Geophysical Journal International*
Manuscript ID:	GJI-S-14-0703
Manuscript Type:	Research Paper
Date Submitted by the Author:	04-Sep-2014
Complete List of Authors:	Tian, Ye; University of Colorado at Boulder, Physics Ritzwoller, Michael; University of Colorado at Boulder, Physics
Keywords:	SEISMOLOGY, Surface waves and free oscillations < SEISMOLOGY, Wave propagation < SEISMOLOGY, Interferometry < GEOPHYSICAL METHODS

Directionality of Ambient Noise on the Juan de Fuca Plate: Implications for Source Locations of the Primary and Secondary Microseisms

Ye Tian and Michael H. Ritzwoller

Center for Imaging the Earth's Interior, Department of Physics, University of Colorado at Boulder, Boulder, CO 80309-0390, USA (ye.tian@colorado.edu)

Abbreviated title: Directionality of Ambient Noise on the JdF Plate

Submitted on: 09/05/2014

Summary

Based on cross-correlations of ambient seismic noise computed from 61 ocean bottom seismometers (OBSs) within the Juan de Fuca plate from the Cascadia Initiative experiment and 42 continental stations near the western US coast, we investigate the locations of generation of the primary (11-20 sec period) and secondary (5-10 sec period) microseisms in the northern Pacific Ocean by analyzing the directionality of the microseism signals received in this region. (1) Ambient noise observed across the array is much different in the primary and secondary microseism bands, both in its azimuthal content and seasonal variation, indicating different source generation locations. (2) The principal secondary microseism signals propagate toward the east, consistent with their generation in deep waters of the North Pacific, perhaps coincident with the region of body wave excitation observed by recent studies. (3) Evidence is presented both for distant primary microseism sources probably in the southern hemisphere as well as local sources within and near the Juan de Fuca plate. Observations of the azimuthal dependence of the amplitude of the fundamental mode Rayleigh wave as well as observations of precursory arrivals in the cross-correlations establish the strongest local generation region lies northwest of the Juan de Fuca plate near the coast of British Columbia perhaps near Graham Island with weaker local sources appearing oceanward of Vancouver Island and southern Oregon. (4) High quality Green's functions are derived from cross-correlations between deep water OBSs and continental stations illustrating that deep water generated signals can efficiently propagate onto the continent and are well recorded by continental seismic stations, at least at periods longer than about 5 sec. In conclusion, the primary and secondary microseisms are generated at different locations, with the secondary microseism dominantly coming from deep-water sources in the northern Pacific and the primary microseism deriving significantly from the shallow waters of the eastern Pacific. These observations suggest different physical mechanisms for generating the two microseisms. The secondary microseisms are likely to be generated by non-linear wave-wave interaction over the deep Pacific Ocean. In contrast, the primary microseism appears to be couple into the solid earth locally in shallow waters from ocean gravity waves but also has a component generated at greater distance of

unknown origin. Above 5 sec period, both microseisms propagate efficiently from either deep or shallow water source regions to continental stations.

Keywords: Seismology, Surface waves and free oscillations, Wave propagation, Interferometry

1. Introduction

In the past decade, tomography based on ambient seismic noise cross-correlations has proven to be a reliable basis for inference of crustal and uppermost mantle structure. It has been successfully applied to many regions across the globe (*e.g., Yao et al.,* 2006; *Lin et al.,* 2007, 2008; *Moschetti et al.,* 2007; *Yang et al.,* 2007, 2010) since its first development by *Shapiro et al.* (2005) and *Sabra et al.* (2005). Compared to traditional methods, ambient noise tomography reduces dependence on earthquakes, extends analysis to shorter periods, and provides higher resolution constraints on Earth's shallow structure.

The reliability of ambient noise tomography relies on the assumption that the ambient noise field becomes approximately homogeneously distributed in azimuth of propagation when averaged over sufficiently long times. In practice, however, noise sources are often heterogeneously distributed (e.g., *Stehly et al.,* 2006; *Yang and Ritzwoller,* 2008) and persistent localized noise sources exist in some places (e.g., *Shapiro et al.,* 2006; *Zeng and Ni,* 2010; *Zheng et al., 2011; Gu and Shen,* 2012). Recent studies have demonstrated that noise source locations and mechanisms can affect the accuracy of tomography obtained from cross-correlations (*Tsai,* 2009; *Weaver et al.,* 2009; *Yao and van der Hilst,* 2009; *Harmon et al.,* 2010). Better knowledge of the mechanism and distribution of ambient noise is of fundamental importance to understand the generation of microseisms, but it is also important to assess the accuracy and reliability of the results from ambient noise tomography.

The generation of microseisms has been studied for over a century. Microseisms were first hypothesized by *Wiechert* (1904) to be generated by surf activities along coasts and studies in the first half of the twentieth century associated them with storm activities. The dominant frequencies of microseisms, however, were observed to be roughly twice the principal ocean gravity wave frequency (the secondary microseism). This observation gave rise to the development of the double frequency wave-wave interaction theory, which was first discussed by (*Miche,* 1944) and extended by *Longuet-Higgins* (1950). *Hasselmann* (1963) extended the double frequency theory to random waves and, furthermore, developed the theoretical basis for microsiesms with frequency content similar to the ocean gravity wave (the

primary microseisms). The theories governing the generation of both primary (~11-20 sec period) and secondary (~3-10 sec period) microseisms have been supported by several recent studies (e.g., *Kibblewhite and Ewans*, 1985; *Kedar et al.*, 2008). In the primary microseism band, most studies infer shallow water sources (e.g., *Hasselmann*, 1963; *Cessaro*, 1994; *Bromirski and Duennebier*, 2002). This is consistent with the theoretical understanding that ocean wave energy transfers into the solid earth by direct coupling in the primary band, which only occurs in relatively shallow regions where the water depth is comparable with the wavelength of the deep water gravity wave (*Hasselmann*, 1963). In the secondary microseism band, generation areas have been observed in both the deep ocean and the shallow water regions in certain locations (*Bromirski et al.*, 2005; *Ardhuin et al.*, 2011; *Kedar*, 2011; *Hillers et al.*, 2012). *Kedar et al.* (2008) and *Ardhuin et al.* (2011) verified with numerical wave modeling that the observed secondary microseisms can be accounted for by wave-wave interaction (*Longuet-Higgins*, 1950) both in the deep ocean with either wind waves or independent wave systems and near the coast with coastal reflected waves. It was, however, suggested by *Bromirski et al.* (2005, 2013) that deep water generated double frequency microseism energy is seldomly recorded by continental stations and land observations are dominated by near-coastal wave activity. Moreover, it is not clear whether the primary and the secondary microseisms share the same shallow water source regions (*Cessaro*, 1994; *Bromirski and Duennebier*, 2002) and persistent noise sources have been observed at different locations across the globe (*Cessaro*, 1994; *Zeng and Ni*, 2010; *Zhan et al.*, 2010; *Gu and Shen*, 2012).

Observations of the source locations based on ambient noise cross-correlations, on the other hand, are as yet quite limited. It is important, however, to make such observations as the pre-cross-correlation normalizations and the time averaging processes tend to obscure the real source distributions and homogenize the intensities of different sources. On a global scale, *Stehly et al.* (2006) and *Yang and Ritzwoller* (2008) investigated the source location of ambient noise using cross-correlations by analyzing data from continental stations located in Europe, Africa, and the western and eastern United States. These studies, although based on similar data, arrived at different conclusions on the source locations, where the former concludes that the primary microseism band is dominated by deep water sources and the secondary

microseism band is mostly affected by shallow water sources, while the latter argues for shallow water sources at all periods based largely on the principle of parsimony. On a regional scale, most studies argue for shallow water sources for both the primary and secondary microseisms (e.g., *Gu et al.*, 2007; *Chen et al.*, 2011; *Köhler et al.*, 2011). *Gu and Shen* (2012), however, made a similar analysis for secondary microseisms in southwestern Canada and observed seismic energy coming from the Pacific Ocean, which is similar to observations in other microseism studies (e.g., *Gerstoft et al.*, 2008; *Landès et al.,* 2010). Enigmatically, they also observed a persistent localized noise source near Lesser Slave Lake. The inconsistent conclusions between these studies are at least partially caused by limitations in the observations used, particularly a lack of observations in the ocean, which could possibly be solved with a combined use of ocean bottom seismometers (OBSs) and near coastal continental stations. The recent deployment of OBSs by the Cascadia Initiative experiment on the Juan de Fuca Plate and the open availability of these data provides such an opportunity to investigate the source locations of microseisms received in this region. The OBS data were the basis for an earlier ambient noise tomographic study of the Juan de Fuca plate performed by *Tian et al.* (2013).

In this paper, we investigate ambient noise cross-correlations obtained from OBSs situated on the Juan de Fuca plate as well as on-land stations located in Washington, Oregon, and Northern California and address the following four questions. First, we consider here whether the primary and secondary microseisms are generated at the same locations by analyzing the directionality of the cross-correlation signals observed in the study area. Second, we investigate whether there are ambient noise signals that are generated in deep waters of the North Pacific. Third, we search for evidence of shallow water sources of ambient noise and determine whether they are continuously or discretely distributed in space. Finally, we investigate the continuity of the microseism wave-fields from the oceanic to the continental parts of the study region by determining whether deep water generated signals recorded on the OBSs propagate onto the continent.

2. Data and Measurements

This study is based on Ocean Bottom Seismograph (OBS) data obtained in the first year of the Cascadia Initiative experiment along with data from EarthScope USArray stations in the western US, as shown in **Figure 1a**. We use data from 61 OBS stations (the vertical channel of station J48A failed during the deployment) together with 42 continental stations near the west coast of the states of Washington, Oregon, and northern California (11 of which are to the east of the region shown in **Fig. 1a**). At least six months of continuous data that overlap in time are available from the 61 OBSs and the 42 continental stations from late November 2011 to early May 2012.

We compute the cross-correlations between vertical component records for all stations after applying traditional ambient noise data processing including running average time-domain normalization and frequency domain normalization (*Bensen et al.*, 2007), such as those shown in **Figure 1b,c**. However, in addition, because of the large number of small earthquakes bordering the Juan de Fuca plate, prior to cross-correlation we further down-weight time intervals when earthquake activity is particularly high. **Figure 1b** shows an example cross-correlation between OBS stations J23A and J47A, which are identified in **Figure 1a**. The frequency-time analysis (FTAN) diagram of the "symmetric component" (the average between positive and negative lags) of the cross-correlation is shown below the cross-correlation with the measured group and phase speed curves indicated, respectively, by white and blue dots. A first-overtone is also observed between periods of 2 and 5 sec, but overtone signals are not used in this study. An example cross-correlation between continental stations I03D and I05D and its FTAN diagram are presented in **Figure 1c** where the group and phase speeds vary less over period in comparison to the oceanic path.

Cross-correlations of ambient noise can be used to determine the azimuthal content of the ambient noise (e.g., *Stehly et al.*, 2006; *Yang and Ritzwoller*, 2008), based on the principle that long-duration cross-correlations are primarily sensitive to opposing waves propagating between the two stations. There are two primary caveats. (1) Time domain normalization tends to accentuate distant sources over local sources. (2) Sources that are not approximately in-line with the two stations produce precursory

signals that may be persistent features of the cross-correlations even for a very long time series. Such precursory signals have been used to study persistent localized sources such as the Gulf of Guinea microseism (*Shapiro et al.*, 2006) and the Kyushu microseism (*Zeng and Ni*, 2010; *Zheng et al.*, 2011). In attempting to ensure that such precursory signals do not interfere with our measurements of the directional dependence of ambient noise, in addition to 'down-weighting' the times of frequent local earthquakes in producing the cross-correlations, we update the FTAN measurements iteratively based on a set of reference group and phase speed dispersion curves. The reference dispersion curves are first generated based on a lithospheric age-speed relationship as described by *Tian et al.* (2013) and then updated after discarding paths that we identify with clear precursory signals. Also, as will be discussed later, precursory signals are observed mainly in the primary microseism band. Measurements affected by strong precursory signals typically still have reasonable surface wave dispersion in the secondary microseism band. Any erroneous measurements in the primary band produce a large jump in the dispersion curve between the two bands which are identified as bad measurements in the FTAN process (*Levshin and Ritzwoller*, 2001).

Because absolute amplitude information is lost during the processing of ambient noise data, we measure only relative Rayleigh wave amplitude by using signal-to-noise ratio (SNR). **Figure 2** illustrates how SNR is measured. We measure SNR in the time domain after narrow band filtering, defining it as the peak signal to the rms trailing noise separately on each lag of the cross-correlation. The two lags represent waves traveling in opposite directions between the two stations where positive lag is associated with waves propagating from the first to the second station in a named station-pair, where the first station is called the “central station”. Our simulations indicate that a SNR > 3 implies that a Rayleigh wave signal exists above the noise level. Other examples of the measurement of SNR in a different frequency band are presented in **Figure 3a**.

For each central station, we sort the cross-correlations into a set of outgoing waves and incoming waves. We plot the SNR for the outgoing waves at the central station and the SNR for the incoming waves at the other stations in the cross-correlations. **Figure 3b** illustrates how the SNR of the outgoing waves can be presented in map

form to display information about the azimuthal content of ambient noise. The orange arrows emanating from station J44A point to the other stations in the cross-correlations, corresponding to outgoing waves. The blue arrows assigned to the neighboring stations point to J44A and correspond to waves coming into that station. Note that for a cross-correlation between two stations A and B, incoming waves for station A are outgoing waves for station B. Thus, all SNR measurements are used, but we assign a measurement to the location of the station for which the measurement corresponds to the outgoing wave. The results for many stations simultaneously are presented in what we call a "fan diagram" (inset diagram on the right in **Fig. 3b**), in which SNR is color-coded and plotted as same-length bars that point in the direction of wave propagation (i.e., away from the source). In producing the fan diagram, we first correct all SNR measurements for geometrical spreading (normalizing to an inter-station distance of 150km), only use stations within 300km of the central station, and normalize all time series lengths (to 180 days). The average SNRs are made for the outgoing wave in overlapping 20 degree bins and are weighted by distance using a spatial Gaussian function with a half width of 150km. Note, in a fan diagram, bars point away from sources of ambient noise. A blue bar means that there is strong microseism noise propagation in the direction to which the bar points. A red bar means that little noise propagates in the direction of the bar.

The principal observations of this paper are presented in **Figures 4** and **5**, which display time-averaged fan diagrams for the primary and secondary microseisms, respectively. These results are averaged spatially for each month and are displayed in **Figures 6** to highlight the monthly variation of ambient noise as well as the azimuthal content and how it varies between continental and oceanic stations in the two microseism bands. A discussion of the content of these diagrams along with implications for potential source regions for both microseism bands is presented in the next section.

3. The Strength and Directionality of Ambient Noise

We discuss here the observations with which we will address the questions that motivate this paper by describing the signal level, the seasonal variation, and the azimuthal content of ambient noise. In doing so, we distinguish between the primary and secondary microseisms as well as continental and oceanic stations where appropriate.

To investigate the directional dependence of microseismic noise in the study area, the stations are grouped spatially into the OBS stations, the northern continental stations (with latitudes greater than 44°), and the southern continental stations. The spatially averaged SNR within each of the three station groups in the primary and the secondary microseism bands are shown in **Figure 6** as a function of month of observation from December 2011 to May 2012. The SNR curves are plotted with cooler colors indicating the northern winter months and warmer colors indicating the northern spring months. Azimuth is defined clockwise from north so that 0° denotes a wave propagating to the north, 90° is for a wave propagating to the east, and so on.

3.1 Signal Level

(1) Ambient noise has a higher SNR on continental than on oceanic stations in both the primary and secondary microseism bands. This is presumably due to higher local noise levels at the oceanic stations, which are incompletely isolated from ocean bottom currents and other sources of local noise. (**Figs. 4, 5, 6**)

(2) Across the Juan de Fuca plate, the SNR decreases toward the continent, which we also believe results from higher local noise levels in shallower waters. This could be caused either by surface gravity waves coupling to the solid earth or ocean bottom currents that are stronger in shallower water. The SNR being lower in the primary than in the secondary microseism band is consistent with surface gravity waves as the primary cause, as they are expected to be stronger in the primary band. (**Figs. 4, 5, 6**)

3.2 Seasonal Variability

(1) For most azimuths on both continental and oceanic stations, ambient noise is stronger in the winter than the spring months. While in every case a peak with stronger signal during spring months exists at azimuths between 0 and 90 degrees. (**Fig. 6**)

(2) The azimuthal content of ambient noise changes less over time in the secondary microseism than the primary microseism band. (**Fig. 6**)

3.3 Azimuthal Content

In each of the six diagrams shown in **Figure 6**, ambient noise SNR peaks at three to four azimuths as marked by color-coded arrows. In each microseism band separately, peaks marked by arrows with the matching color correspond to waves that are potentially from the same source region as will be discussed later and illustrated with **Figures 7 - 10**. The back-projected paths and the potential source locations of these peaks will be discussed in the next section.

(1) Ambient noise appears to propagate in all directions (SNR > 5) at both oceanic and continental stations in both microseism bands (**Figs. 6**).

(2) The red, green, and blue arrows in the primary microseism band as well as the red and green arrows in the secondary microseism band mark the azimuths with stronger noise during the winter months, while the yellow peaks in both period bands mark stronger noise during the spring.

(3) For the secondary microseism, the azimuthal distribution of ambient noise is temporally and spatially stable for both the OBS and continental stations. The strongest energy is observed continuously in the azimuth range between the red and the yellow arrows, which is associated with waves propagating generally to the east (**Figs. 6d, e, f**). The green peak is not observed on OBSs and is much smaller in SNR compared to the other two peaks.

(4) For the primary microseism, the four peaks marked by arrows are well separated azimuthally. The directionality of the green and yellow arrows are stable across the

three station groups, while the azimuth marked by the red arrows rotates by 15 to 30 degrees between station groups. The blue peak is observable only on the OBS stations and the southern continental stations (and might be merged with another peak on the northern continental stations) and rotates by more than 140 degrees when observed on the two station groups.

4. Discussion

Four questions motivate this paper, which we now discuss based on the observations presented in the earlier sections.

4.1 Are the primary and secondary microseisms generated at the same locations?

As shown in **Figure 6** and as is illustrated further in **Figures 7-10**, ambient noise is much different in the primary and secondary microseism bands, both in its azimuthal content and seasonal variation. The propagation of the secondary microseism, both on the continent and within the ocean, is principally eastward and displays little seasonal variation. In contrast, the azimuthal content of the primary microseism on the Juan de Fuca plate and the northern and southern parts of the continent differ from one another. The azimuthal content of ambient noise varies over time on the continent, with stronger propagation to the southeast and southwest during the winter and to the northeast during the summer. These observations imply well separated locations of generation of the primary and secondary microseisms. As discussed further below, the secondary microseism appears to be generated far from the observing networks, in the open ocean of the northern Pacific, and the primary microseism appears to be derived both locally, in the shallower waters of the northeastern Pacific, and distantly, possibly from locations over broad regions of the Pacific and northern Atlantic Oceans.

4.2 Are ambient noise signals generated in deep water of the North Pacific?

The principal direction of ambient noise in the secondary microseism band is generally to the east, as observed both in the ocean and on the continent and for all months considered. **Figure 7d** illustrates this by back-projecting the wave propagation paths for the red, green, and yellow peaks shown in **Figure 6d,e,f**. Paths with the same color are almost perpendicular to each other in **Figure 7d**, indicating distant source locations, although the mean SNR is considerably higher on the continent. As shown in **Figure 7a,b,c**, strong time-averaged energy is observed continuously between the red and the yellow arrows and the azimuthal content is similar on the continent and in the ocean, indicating that the source region(s) are likely to be the same and distant from the observing points.

Figure 8 presents great circle paths back-projected from the OBS locations on a larger area map. Azimuths between the red and yellow arrows (~45°-130°) from **Figure 7** are indicated with black lines. The strongest observed signal, which occurs at wave propagation azimuths around 120° (near the red arrows), agrees well with the source regions hypothesized by *Gerstoft et al.* (2008) and *Landès et al.* (2010) for body waves (marked with orange and yellow ellipses). The second strongest signal in the secondary band occurs at azimuths around 60° (near the yellow arrows), which is outside of these regions. However, *Kedar et al.* (2008) predicts a diffuse intense region of wave-wave interaction in the northern Pacific Ocean (marked with a green ellipse), which is weakened after multiplying by the microseismic excitation potential. *Landès et al.* (2010) also observed a weaker source region in the central Pacific Ocean (marked with a yellow dashed ellipse). It is possible that the 60° signal that we observe is generated in these regions.

The seasonal characteristics of the 60° (near the yellow arrows) and 120° (near the red arrows) peaks (**Figure 6d,e,f**) are different from one another. The 60° signal is slightly stronger during the spring months while at 120° the signal is strongest for the winter months. This is consistent with the assumption that the energy propagating at 120° is produced by storm activities over the deep North Pacific Ocean, which is stronger during the northern winter months (*Gerstoft et al.*, 2008; *Landès et al.*, 2010), while the 60° energy is produced over the Central Pacific Ocean, which is expected to have less seasonal variability.

The strongest secondary microseism source in the Northern Hemisphere during the winter months is predicted to be near the southern tip of Greenland by *Kedar et al.* (2008) and *Ardhuin et al.* (2011). The propagation direction of waves from this source agrees well with the observed green peaks on **Figure 6e,f** and **Figure 7b,c** with the propagation direction shown in **Figure 7d**.

In summary, our observations are consistent with deep water generation of the secondary microseism perhaps coincident with the regions of body wave excitation inferred by *Gerstoft et al.* (2008) and *Landès et al.* (2010). The azimuthal content of the primary microseism is more complicated and not as easily explained with a small set of deep water source regions as the secondary microseism. In fact, the primary

microseism appears to be generated in different areas than the secondary microseism. We discuss the possible source regions of the primary microseism in the next subsection.

4.3 Are ambient noise signals generated locally in shallow waters on the Juan de Fuca Plate and its surroundings?

Figure 9 presents time-averages of the four primary microseism peaks observed across the three station groups and their back-projected paths. A more complicated picture emerges than for the secondary microseism, including what we interpret as evidence for both distant and relatively local sources. Four observations are particularly noteworthy.

(1) The green arrows in **Figure 9d** correspond to directions similar to those observed in the secondary microseism band (**Figure 7d**). We believe that this signal is caused by a North Atlantic source, as the back-projection in **Figure 10** (green region) indicates. But, the source region or regions are too distant for us to determine if the primary and secondary microseisms are being generated in the same or different locations.

(2) The yellow arrows in **Figure 9d** indicate a Pacific source. The peak at the OBS stations (**Fig. 9a**) is much weaker than for the continental stations but is well observed in **Figure 6a** in the spring. Because the yellow arrows in **Figure 9d** are not parallel to one another, this source may be considered to be relatively close. However, because of relatively low signal-to-noise level, the azimuthal content for these peaks is not precise and, as **Figure 6** illustrates, this wave is stronger in the northern spring than winter months. Therefore, we believe that it is likely that this source is distant and in the southern hemisphere. **Figure 10** presents the back-projection of the azimuths observed, illustrating that a broad area of the southern Pacific is potentially consistent for generating these signals. We cannot determine if there is a deep water or shallow water source region.

(3) The three red paths in **Figure 9d** intersect in the shallow water regions to the northwest of the Juan de Fuca plate, and we believe that these peaks in the primary microseism band are generated relatively locally in shallow waters. The intersection

point is approximate and should not be interpreted to convey the source location accurately, but our estimate lies between the coast of British Columbia and Graham Island. The water depth in much of this area is shallower than 50 m and shallower still near Graham Island. The wavelength of the deep water gravity wave, given by the Airy wave theory ($\lambda = gT^2/2\pi$, where g is the gravitational acceleration and T is the period), is between 190 and 620 m for the primary microseism band (11 – 20 sec). Thus, the water depth within this area satisfies the theoretical requirement for ocean wave energy to transfer into the solid earth by direct coupling, which mostly occurs where the water depth is within 1/4 wavelength of the deep water gravity wave (Hasselmann, 1963; Bromirski and Duennebier, 2002).

(4) The amplitude of the curves near the blue arrows are weaker compared to near the red arrows, is not observed on the northern continental stations and its directionality is complicated, as seen in **Figure 9d**. We believe that this peak also originates locally in shallow waters, probably off the southern Oregon coast. Even though this signal is not obviously evident in the azimuthal plots such as those in **Figure 9**, it may be indicated by precursory signals, which we discuss now.

Besides the SNR of the observed surface wave signals, clear systematic precursory arrivals are observed for many station pairs. These observations produce complementary evidence about the location of some microseism sources. **Figure 11** presents an example of such a precursory signal on the cross-correlation of the station-pair J42A-I05D. Strong precursors appear near zero time on both the broadband and the primary microseism signals, but disappear when filtered into the secondary microseism band. Thus, such precursors are nearly entirely in the primary band. The time and duration of the precursor observed on this station pair is consistent with the source location identified by the blue ellipse in **Figure 12a**. Systematic observations on precursors from this source and 2 other source locations are presented in **Figure 12** with two cross-correlation record sections centered at the continental stations B05D and I05D. All presented cross-correlations are between OBS and continental stations and are filtered in the period band 0.06 – 0.085 Hz (within the primary microseism band) in which the precursory signals are particularly strong.

The fact that the precursory signals appear in a systematic way in these record sections indicates that they are generated by localized sources and more than one such source region is needed. To test this conclusion we assume three potential source regions as marked by red, green and blue ellipses in **Figure 12a**, off the coast of northern British Columbia (red), near Vancouver Island (green), and off the southern Oregon coast (blue). We then predict the arrival times of the precursory signals that would be generated on cross-correlations of ambient noise based on a simple group velocity model as indicated by the background color in **Figure 12a** (group velocity, ocean: 3.4 km/s, continent: 2.5 km/s), which has been determined by averaging the measurements made on oceanic and continental paths in this region. The red, green and blue ellipses in the record sections (**Fig. 12b,c**) indicate the predicted arrival times with colors associated with the three source regions. Note that the duration of the predicted precursory arrival window is a function of the geometrical relation between the interstation path and the spatial extent of the source region. A larger source region tends to produce a larger precursory window, on average, but would not cause a wider window if the sources align with a hyperbola whose foci are the 2 station locations. The orange lines indicate arrival times of the fundamental Rayleigh waves in the cross-correlations, the non-precursory signals, predicted with a group velocity of 3 km/sec.

The predictions match most of the observed precursory signals regardless of the fact that the group speed model is an over simplification. On cross-correlations centered at station I05D, which is located in Central Oregon, the strongest precursory arrivals match predictions from the blue source region. Cross-correlations centered on station B05D, on the other hand, are more sensitive to energy from the red and green sources due to proximity. This suggests that the signals produced in these source regions are probably scattered and the direct arrival decays quickly with distance. The locations of the red and blue source regions agree well with the azimuthal content of the fundamental surface waves as shown in **Figure 9**. The green source region, however, is not easily identified through its azimuthal dependence as it is possibly merged in azimuth with peaks from other source regions. The observed shallow water source locations and the discontinuity of sources along the coastline are consistent with earlier studies that have argued that the primary microseism sources are limited to certain coastal locations (e.g., *Cessaro*, 1994; *Bromirski and Duennebier*, 2002).

A large number of small earthquakes (magnitude 3 to 4) occurred near Graham Island and on the Explorer Plate, along the Blanco fracture zone, the Gorda Ridge, and the Mendocino fracture zone in the time period in which our cross-correlations are computed. Therefore, in principal, the precursory signals we observe may be earthquake generated. We believe, however, that this is not the case for two major reasons. (1) Precursory signals we observe are strongest in the primary microseism band and are largely not present in the secondary microseism band. This is opposite of what would be expected if small local earthquakes were the source of the precursory arrivals. (2) The precursory signals associated with the blue ellipses on the record sections are fit far better if we set the source region to be along the southern Oregon coastline rather than shifting it westward where the majority of small earthquakes occurs. Nonetheless, the amplitudes of the precursory signals, especially those associated with the blue source region, are affected by surrounding small earthquakes. "Precursor-to-Noise Ratios" (PNRs) decay with the source-station distances in the expected way for the red and green source regions but for the blue source region do not show a clear decay.

As with the azimuthal content of the Rayleigh waves in the cross-correlations, the use of the arrival times of precursory signals is not a highly accurate means to determine source locations. Therefore, source regions other than the three discussed may exist. An example of signals that are not accounted for can be seen in **Figure 12b** on the positive lags where signals with large amplitudes arrive after the fundamental mode Rayleigh wave. These 'post-cursory' signals could arise either due to multiple scattering of surface wave energy or where large gradients exist in the local group speed structure. The ocean-continent boundary is a good example of such a structure and the presence of the 'post-cursory signals' in our observations may indicate source generation along the coastline farther to the northwest of the study area near, for example, the Gulf of Alaska. A formal analysis of the post-cursors, however, is beyond the scope of this paper. Moreover, the Rayleigh wave arrivals could be merged with the precursory signals produced by these localized sources, such as those shown in **Figure 12b**. Thus, additional de-noising processing may be needed for studies aiming to investigate the shallow velocity structure in this region.

In conclusion, local primary microseism sources are indicated by observations from the azimuthal dependence of the fundamental mode Rayleigh wave SNRs as well as observations from precursory signals. The strongest local generation region is observed to the northwest of the Juan de Fuca plate near the coast of British Columbia perhaps near Graham Island. Two weaker generation regions are observed in shallow waters near the western US coastline, one near Vancouver Island and another along the coastline of southern Oregon.

4.4 Does the ambient noise wavefield extend from the oceanic to the continental parts of the study region?

To show that the deep-water generated microseisms observed in this study do propagate onto the continent, we present in **Figure 13** five example cross-correlations along the west-east path between OBS stations J47A, J37A, J356A, and J33A and continental station I05D. Three of these are between oceanic stations: J47A-J37A, J47A-J35A, and J47A-J33A. The other two are from oceanic to continental stations: J33A-I05D and J47A-I05D. Station J47A is located well out of the shallow water region about 400 kilometers from the coastline where water depth is over 2500 meters. The locations of the five paths are indicated by black arrows in **Figure 13a** and the positive lags of the corresponding cross-correlations and their FTAN diagrams are presented in **Figure 13b-f**. The measured group and phase velocity dispersion curves are indicated by white and blue dots, respectively.

On cross-correlations near the Juan de Fuca Ridge, as shown in **Figure 13b,c** for station pairs J47A-J37A and J47A-J35A, clear fundamental mode Rayleigh wave signals are observed in a period range that extends to as low as 4 sec. Longer period measurements (>15sec) are missing from the station pair J47A-J37A because of the three-wavelength criterion (Benson, 2008), but longer periods are well observed on station pair J47A-J35A. Cross-correlations to stations located in shallow waters near the coastline, however, appear to be much noisier, especially in the primary microseism band. **Figure 13d,e** show two examples of such cross-correlations, one on the oceanic side between station pair J47A-J33A and the other on the continental side between station pair J33A-I05D. The contamination is probably from tilting and compliance noise in the shallow ocean as described by *Webb and Crawford* (1999)

and *Crawford and Webb* (2000). Such noise largely disappears for cross-correlations from deep water to the continent, as shown in **Figure 13f**. Fairly good fundamental mode dispersion is observed between 5 and 30 sec period on the station pair J47A-I05D, although signals in the secondary microseism band appear to be weaker.

We conclude, therefore, that in both the primary and secondary microseism bands, deep-water generated microseisms efficiently propagate onto the continent and are recorded by seismic stations. The shallow water stations appear to be contaminated by strong local noise and de-noise techniques (e.g., *Webb and Crawford*, 1999; *Crawford and Webb*, 2000) may be necessary to extract the ambient noise signal in these regions. Below 5 sec period, however, no signals are observed between the deep oceanic and continental stations, which is probably due to scattering attenuation (and perhaps anelastic attenuation) at the transition across the continental-shelf boundary as discussed by *Bromirski et al.* (2013).

4. Conclusions

We investigate the source locations of the primary and secondary microseism signals based on cross-correlations of the vertical components of 61 ocean bottom seismometers (OBSs) located on the Juan de Fuca Plate from the Cascadia Initiative experiment and 42 continental stations situated in the Pacific Northwest near the US coast. Ambient noise observed across the array is much different in the primary and secondary microseism bands, both in its azimuthal content and seasonal variation, indicating different source generation locations.

In the secondary microseism band, the principal signals propagate to the east and display little seasonal variation both on the continent and on the ocean bottom. Observed azimuthal contents are consistent with source generation in deep water of the North Pacific, which is possibly coincident with the region of body wave excitation observed by *Gerstoft et al.* (2008) and *Landès et al.* (2010).

In the primary microseism band, the observed azimuthal contents on the Juan de Fuca Plate and the northern and southern parts of the continent arrays differ from one another. Strong seasonal variations are observed in all three regions. Waves propagating to the northeast are stronger during the northern spring, indicating possible distant sources from the south Pacific, while waves propagating to the south and east are stronger during the northern winter months. We infer the existence of local sources from observations of the azimuthal dependence of the fundamental mode Rayleigh wave SNRs as well as observations of precursory signals. The strongest local generation region is inferred to lie to the northwest of the Juan de Fuca Plate near the coast of British Columbia, perhaps near Graham Island. Two weaker generation regions are observed in shallow waters near the western US coastline, one near Vancouver Island and another along the southern coastline of Oregon.

The observed locations of generation of the primary and secondary microseisms agree well with the theories proposed by *Longuet-Higgins* (1950) and *Hasselmann* (1963). The secondary microseisms are dominated by deep-water sources in the northern Pacific, which are likely to be due to non-linear wave-wave interaction either with wind waves or between independent wave systems over the deep Pacific Ocean. In contrast, primary microseisms are derived significantly from the local shallow waters

of the eastern Pacific, which suggest direct coupling of ocean gravity waves into the shallow ocean bottom as the generation mechanism. Additionally, primary microseism energy appears to derive from distant sources of unknown origin in North Atlantic and Southern Pacific hemisphere.

Finally, high quality ambient noise empirical Green's functions derived from the ambient noise cross-correlations are observed between continental stations and deep water OBSs, which illustrates that deep water generated seismic surface waves do efficiently propagate onto the continent and are well recorded by continental seismic stations at least above 5 sec period.

Acknowledgments

The authors are grateful to the Cascadia Initiative Expedition Team for acquiring the Amphibious Array Ocean Bottom Seismograph data and appreciate the open data policy that made the data available shortly after they were acquired. The facilities of the IRIS Data Management System were used to access some of the data used in this study. The IRIS DMS is funded through the US National Science Foundation under Cooperative Agreement EAR-0552316. This work utilized the Janus supercomputer, which is supported by the National Science Foundation (award number CNS-0821794), the University of Colorado Boulder, the University of Colorado Denver, and the National Center for Atmospheric Research. The Janus supercomputer is operated by the University of Colorado Boulder.

References

Ardhuin, F., E. Stutzmann, M. Schimmel, and A. Mangeney (2011), Ocean wave sources of seismic noise, *J. Geophys. Res. Oceans 1978–2012*, *116*(C9).

Bensen, G. D., M. H. Ritzwoller, M. P. Barmin, A. L. Levshin, F. Lin, M. P. Moschetti, N. M. Shapiro, and Y. Yang (2007), Processing seismic ambient noise data to obtain reliable broad-band surface wave dispersion measurements, *Geophys. J. Int.*, *169*(3), 1239–1260, doi:10.1111/j.1365-246X.2007.03374.x.

Bromirski, P. D., and F. K. Duennebier (2002), The near-coastal microseism spectrum: Spatial and temporal wave climate relationships, *J. Geophys. Res.*, *107*(B8), 2166.

Bromirski, P. D., F. K. Duennebier, and R. A. Stephen (2005), Mid-ocean microseisms, *Geochem. Geophys. Geosystems*, *6*(4), Q04009.

Bromirski, P. D., R. A. Stephen, and P. Gerstoft (2013), Are deep-ocean-generated surface-wave microseisms observed on land?, *J. Geophys. Res. Solid Earth*, *118*(7), 3610–3629.

Cessaro, R. K. (1994), Sources of primary and secondary microseisms, *Bull. Seismol. Soc. Am.*, *84*(1), 142–148.

Chen, Y.-N., Y. Gung, S.-H. You, S.-H. Hung, L.-Y. Chiao, T.-Y. Huang, Y.-L. Chen, W.-T. Liang, and S. Jan (2011), Characteristics of short period secondary microseisms (SPSM) in Taiwan: The influence of shallow ocean strait on SPSM: SPSM EXCITATIONS IN OFFSHORE TAIWAN, *Geophys. Res. Lett.*, *38*(4), n/a–n/a, doi:10.1029/2010GL046290.

Crawford, W. C., and S. C. Webb (2000), Identifying and removing tilt noise from low-frequency (< 0.1 Hz) seafloor vertical seismic data, *Bull. Seismol. Soc. Am.*, *90*(4), 952–963, doi:10.1785/0119990121.

Gerstoft, P., P. M. Shearer, N. Harmon, and J. Zhang (2008), Global P, PP, and PKP wave microseisms observed from distant storms, *Geophys. Res. Lett.*, *35*(23).

Gu, Y. J., and L. Shen (2012), Microseismic Noise from Large Ice-Covered Lakes?, *Bull. Seismol. Soc. Am.*, *102*(3), 1155–1166, doi:10.1785/0120100010.

Gu, Y. J., C. Dublanko, A. Lerner-Lam, K. Brzak, and M. Steckler (2007), Probing the sources of ambient seismic noise near the coasts of southern Italy, *Geophys. Res. Lett.*, *34*(22), doi:10.1029/2007GL031967.

Harmon, N., C. Rychert, and P. Gerstoft (2010), Distribution of noise sources for seismic interferometry, *Geophys. J. Int.*, *183*(3), 1470–1484.

Hasselmann, K. (1963), A Statistical Analysis of the Generation of Microseisms, *Rev. Geophys.*, *1*(2), 177–210, doi:10.1029/RG001i002p00177.

Hillers, G., N. Graham, M. Campillo, S. Kedar, M. Landès, and N. Shapiro (2012), Global oceanic microseism sources as seen by seismic arrays and predicted by wave action models, *Geochem. Geophys. Geosystems*, *13*(1).

Karim G. Sabra, Peter Gerstoft, Philippe Roux, and W. A. Kuperman (2005), Extracting time-domain Green's function estimates from ambient seismic noise, *Geophys. Res. Lett.*, *32*(3), doi:10.1029/2004GL021862.

Kedar, S. (2011), Source distribution of ocean microseisms and implications for time-dependent noise tomography, *Comptes Rendus Geosci.*, *343*(8), 548–557.

Kedar, S., M. Longuet-Higgins, F. Webb, N. Graham, R. Clayton, and C. Jones (2008), The origin of deep ocean microseisms in the North Atlantic Ocean, *Proc. R. Soc. Math. Phys. Eng. Sci.*, *464*(2091), 777–793.

Kibblewhite, A., and K. Ewans (1985), Wave-Wave Interactions, Microseisms, and Infrasonic Ambient Noise in the Ocean, *J. Acoust. Soc. Am.*, *78*(3), 981–994, doi:10.1121/1.392931.

Köhler, A., C. Weidle, and V. Maupin (2011), Directionality analysis and Rayleigh wave tomography of ambient seismic noise in southern Norway: Ambient noise tomography of southern Norway, *Geophys. J. Int.*, *184*(1), 287–300, doi:10.1111/j.1365-246X.2010.04830.x.

Landès, M., F. Hubans, N. M. Shapiro, A. Paul, and M. Campillo (2010), Origin of deep ocean microseisms by using teleseismic body waves, *J. Geophys. Res. Solid Earth 1978–2012*, *115*(B5).

Levshin, A. L., and M. H. Ritzwoller (2001), Automated detection, extraction, and measurement of regional surface waves, in *Monitoring the Comprehensive Nuclear-Test-Ban Treaty: Surface Waves*, pp. 1531–1545, Springer.

Lin, F.-C., M. H. Ritzwoller, J. Townend, S. Bannister, and M. K. Savage (2007), Ambient noise Rayleigh wave tomography of New Zealand, *Geophys. J. Int.*, *170*(2), 649–666, doi:10.1111/j.1365-246X.2007.03414.x.

Lin, F.-C., M. P. Moschetti, and M. H. Ritzwoller (2008), Surface wave tomography of the western United States from ambient seismic noise: Rayleigh and Love wave phase velocity maps, *Geophys. J. Int.*, *173*(1), 281–298.

Longuet-Higgins, M. S. (1950), A theory of the origin of microseisms, *Philos. Trans. R. Soc. Lond. Ser. Math. Phys. Sci.*, *243*(857), 1–35.

Miche, R. (1944), *Mouvements ondulatoires de la mer en profondeur constante ou décroissante forme limite de la houle lors de son déferlement, application aux digues maritimes*, Paris.

Moschetti, M. P., M. H. Ritzwoller, and N. M. Shapiro (2007), Surface wave tomography of the western United States from ambient seismic noise: Rayleigh wave group velocity maps: U.S. SURFACE WAVE TOMOGRAPHY, *Geochem. Geophys. Geosystems*, *8*(8), n/a–n/a, doi:10.1029/2007GC001655.

Sabra, K. G., P. Gerstoft, P. Roux, W. A. Kuperman, and M. C. Fehler (2005), Surface wave tomography from microseisms in Southern California: SURFACE WAVE TOMOGRAPHY, *Geophys. Res. Lett.*, *32*(14), n/a–n/a, doi:10.1029/2005GL023155.

Shapiro, N. M., M. Campillo, L. Stehly, and M. H. Ritzwoller (2005), High-resolution surface-wave tomography from ambient seismic noise, *Science*, *307*(5715), 1615–1618, doi:10.1126/science.1108339.

Shapiro, N. M., M. H. Ritzwoller, and G. D. Bensen (2006), Source location of the 26 sec microseism from cross-correlations of ambient seismic noise, *Geophys. Res. Lett.*, *33*(18), doi:10.1029/2006GL027010.

Stehly, L., M. Campillo, and N. M. Shapiro (2006), A study of the seismic noise from its long-range correlation properties, *J. Geophys. Res. Solid Earth 1978–2012*, *111*(B10).

Tian, Y., W. Shen, and M. H. Ritzwoller (2013), Crustal and uppermost mantle shear velocity structure adjacent to the Juan de Fuca Ridge from ambient seismic noise, *Geochem. Geophys. Geosystems*, *14*(8), 3221–3233, doi:10.1002/ggge.20206.

Tsai, V. C. (2009), On establishing the accuracy of noise tomography travel-time measurements in a realistic medium, *Geophys. J. Int.*, *178*(3), 1555–1564.

Weaver, R., B. Froment, and M. Campillo (2009), On the correlation of non-isotropically distributed ballistic scalar diffuse waves, *J. Acoust. Soc. Am.*, *126*(4), 1817, doi:10.1121/1.3203359.

Webb, S. C., and W. C. Crawford (1999), Long-period seafloor seismology and deformation under ocean waves, *Bull. Seismol. Soc. Am.*, *89*(6), 1535–1542.

Wiechert, E. (1904), Discussion, Verhandlung der zweiten Internationalen Seismologischen Konferenz, *Beitrage Zur Geophys.*, *2*, 41–43.

Yang, Y., and M. H. Ritzwoller (2008), Characteristics of ambient seismic noise as a source for surface wave tomography, *Geochem. Geophys. Geosystems*, *9*(2), Q02008.

Yang, Y., M. H. Ritzwoller, A. L. Levshin, and N. M. Shapiro (2007), Ambient noise Rayleigh wave tomography across Europe, *Geophys. J. Int.*, *168*(1), 259–274.

Yang, Y. et al. (2010), Rayleigh wave phase velocity maps of Tibet and the surrounding regions from ambient seismic noise tomography: RAYLEIGH WAVE PHASE VELOCITIES IN TIBET, *Geochem. Geophys. Geosystems*, *11*(8), n/a–n/a, doi:10.1029/2010GC003119.

Yao, H., and R. D. van der Hilst (2009), Analysis of ambient noise energy distribution and phase velocity bias in ambient noise tomography, with application to SE Tibet, *Geophys. J. Int.*, *179*(2), 1113–1132, doi:10.1111/j.1365-246X.2009.04329.x.

Yao, H., R. D. van Der Hilst, and M. V. De Hoop (2006), Surface-wave array tomography in SE Tibet from ambient seismic noise and two-station analysis–I. Phase velocity maps, *Geophys. J. Int.*, *166*(2), 732–744.

Zeng, X., and S. Ni (2010), A persistent localized microseismic source near the Kyushu Island, Japan: PL MICROSEISMIC SOURCE NEAR KYUSHU, *Geophys. Res. Lett.*, *37*(24), n/a–n/a, doi:10.1029/2010GL045774.

Zhan, Z., S. Ni, D. V. Helmberger, and R. W. Clayton (2010), Retrieval of Moho-reflected shear wave arrivals from ambient seismic noise: SmS reflections from seismic noise, *Geophys. J. Int.*, no–no, doi:10.1111/j.1365-246X.2010.04625.x.

Zheng, Y., W. Shen, L. Zhou, Y. Yang, Z. Xie, and M.H. Ritzwoller (2011), Crust and uppermost mantle beneath the North China Craton, northeastern China, and the Sea of Japan from ambient noise tomography, *J. Geophys. Res.,* 116, B12, 1978, 2013.

Figure 1

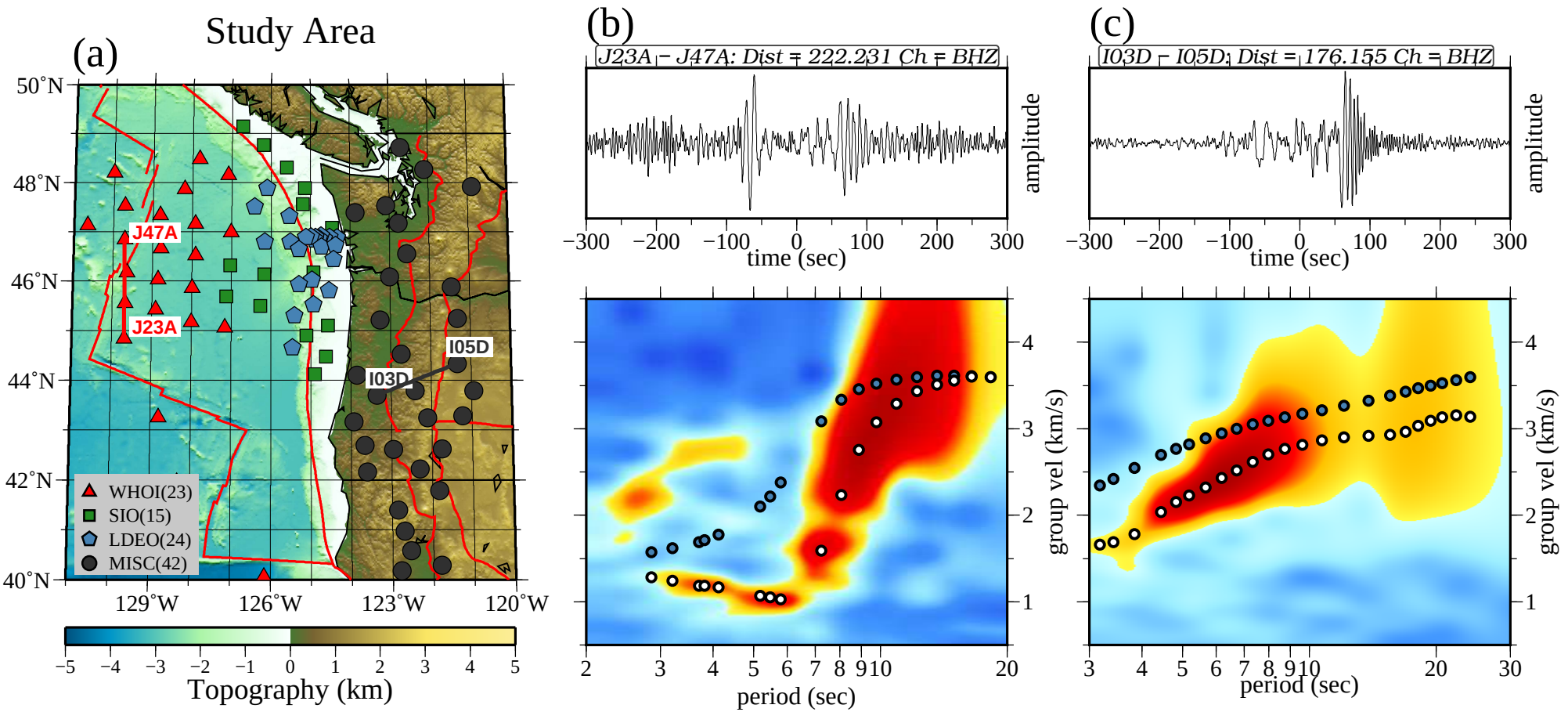

Figure 1. (a) Locations of the 62 Cascadia Initiative OBS stations are plotted over bathymetry/topography with the Juan de Fuca Ridge, the plate boundary, and continental tectonic regions shown as red lines. OBS stations from three different institutions are plotted with red triangles (WHOI), green squares (SIO), and blue pentagons (LDEO) while the continental stations are plotted with gray circles. (b) Example six month cross-correlation of vertical component ambient noise between stations J23A and J47A, marked as the red interstation path in Fig. 1a, and the corresponding symmetric component group velocity versus period (FTAN) diagram. Background color indicates the spectral amplitude and the group and phase speeds are indicated with white and blue circles, respectively. A 1st overtone signal is seen between 2 - 5 sec periods with group speeds between 2 and 3 km/sec. (c) Same as (b), but for continental stations I03D and I05D, marked as the grey interstation path in Fig. 1a.

Figure 2

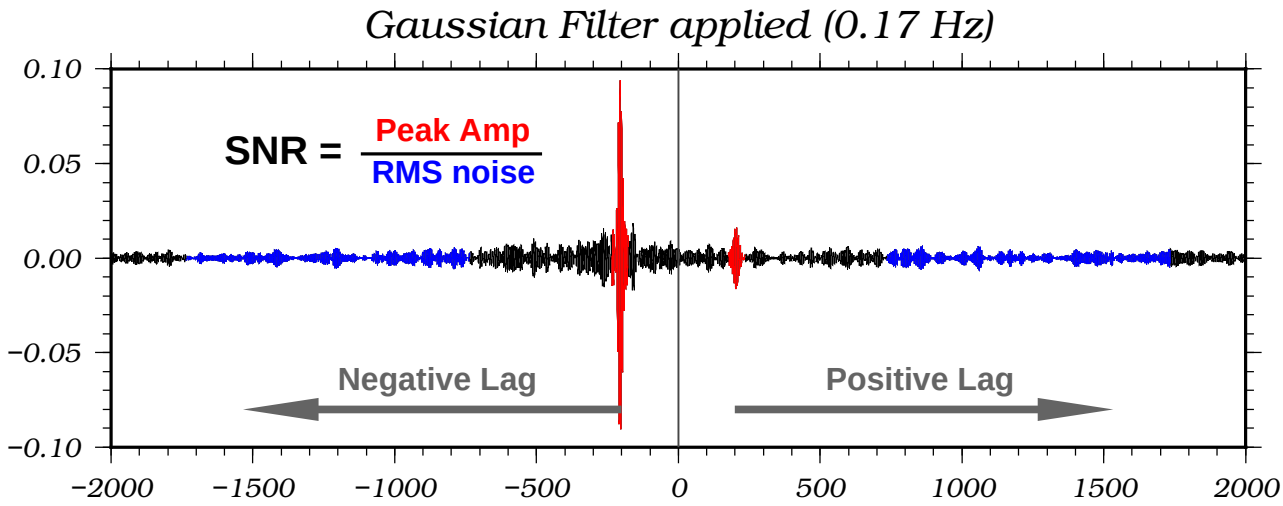

Figure 2. Illustration of the measurement of signal-to-noise ratio (SNR). The ambient noise cross-correlation between OBS stations J30A and J44A (identified in Fig. 3b) is filtered around center frequency 0.17 Hz in the secondary microseism band. The signal windows are centered on the Rayleigh wave group time measured by frequency-time analysis (FTAN) and are marked in red. The noise windows begin 500 seconds after the signal, are 1000 seconds in duration, and are marked in blue. The SNR is defined as the peak amplitude in the signal window divided by the root-mean-square of the amplitude in the noise window, and is computed for a set of center frequencies.

Figure 3

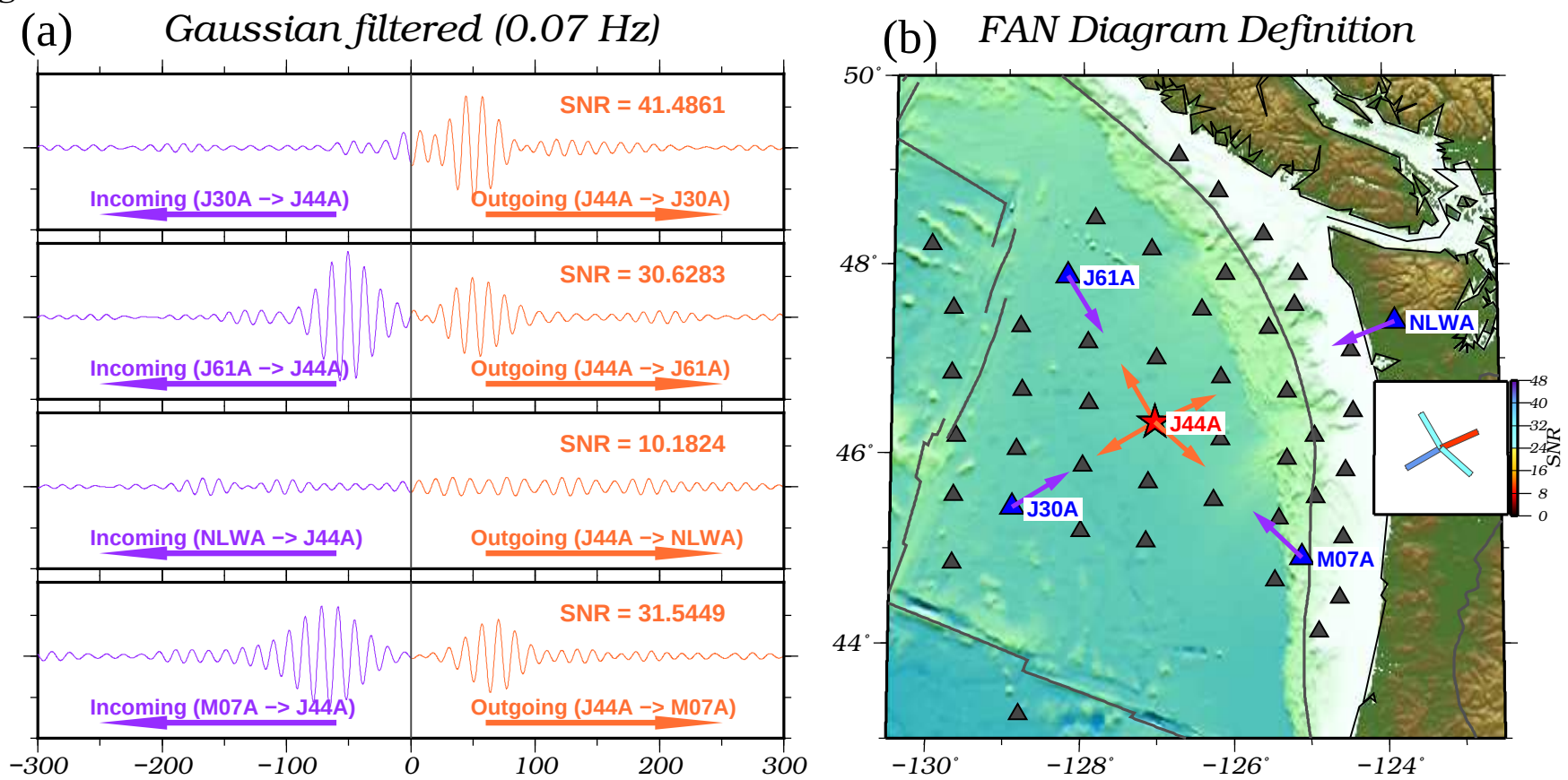

Figure 3. Illustration of the construction of outgoing SNR maps, called fan diagrams. (a) Cross-correlations between OBS station J44A and four nearby stations with a Gaussian filter applied around 0.07 Hz (primary microseism). The positive correlation lags relate to outgoing waves from station J44A, colored orange, and the incoming waves are on the negative correlation lags, colored blue. The SNR measurements for the outgoing waves at 0.07 Hz are indicated. (b) The locations of the center station J44A and the four nearby stations are plotted, respectively, as the red star and blue triangles. Orange arrows show the outgoing wave propagation directions and are assigned to the center station, whereas the blue arrows are the incoming wave directions and are assigned to the nearby stations. Only outgoing SNRs are presented and are summarized using “fan diagrams” as exemplified by the inset diagram on the right. The SNR is plotted as same-length colored bars pointing in the direction of the inter-station azimuth (in the direction of wave propagation away from the source) such that blue colors indicate a higher SNR than red colors.

Figure 4

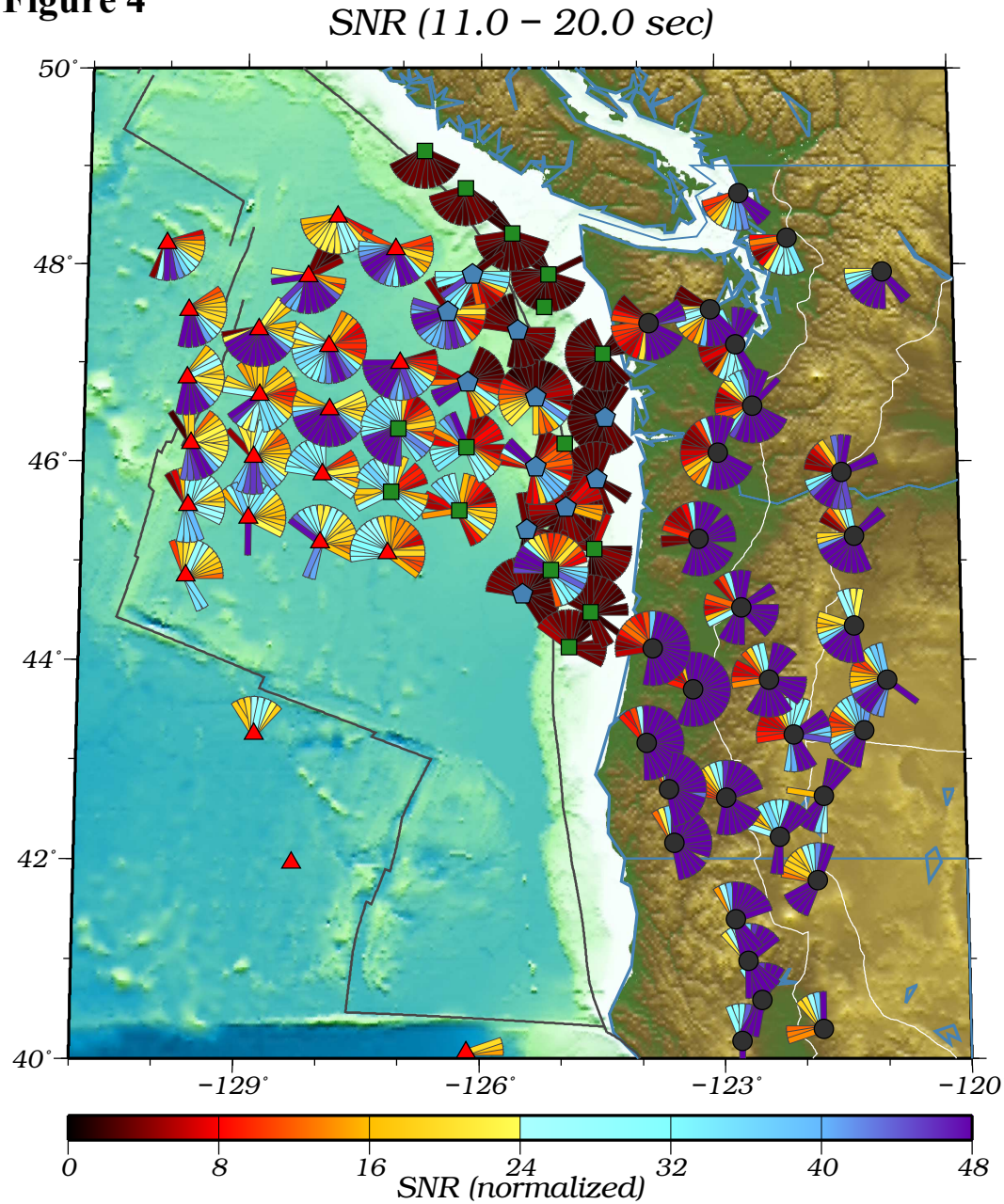

Figure 4. The principal measurements in the paper are presented here and in Fig. 5. Fan diagrams (see Fig. 3 for definition) of outgoing wave amplitudes are plotted at each station for the primary microseism band (11-20 sec period). Cooler colors represent higher SNR and point in the direction of propagation (away from the source).

Figure 5

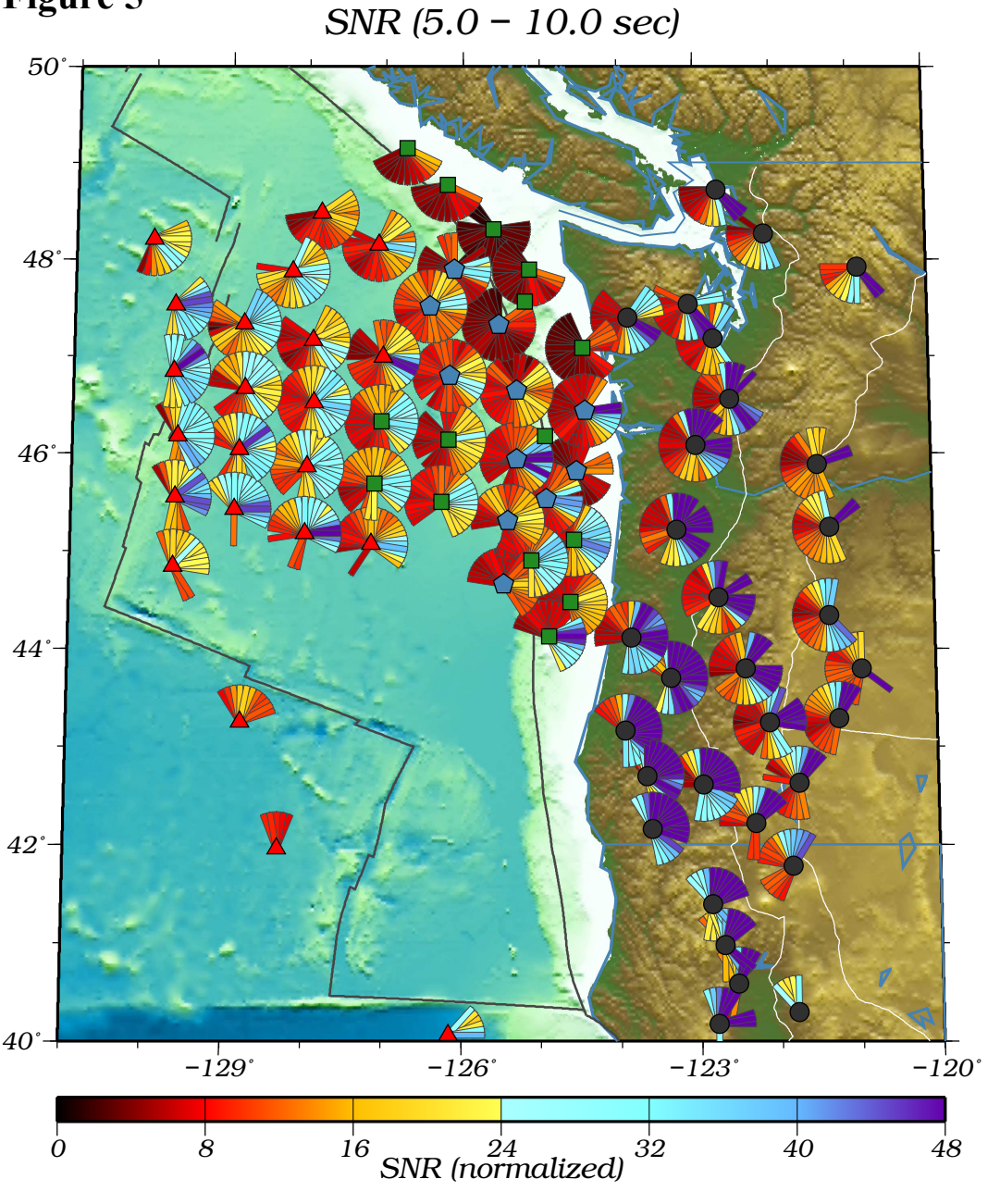

Figure 5. Same as Fig. 4, but for the secondary microseism band (5-10 sec period).

Figure 6

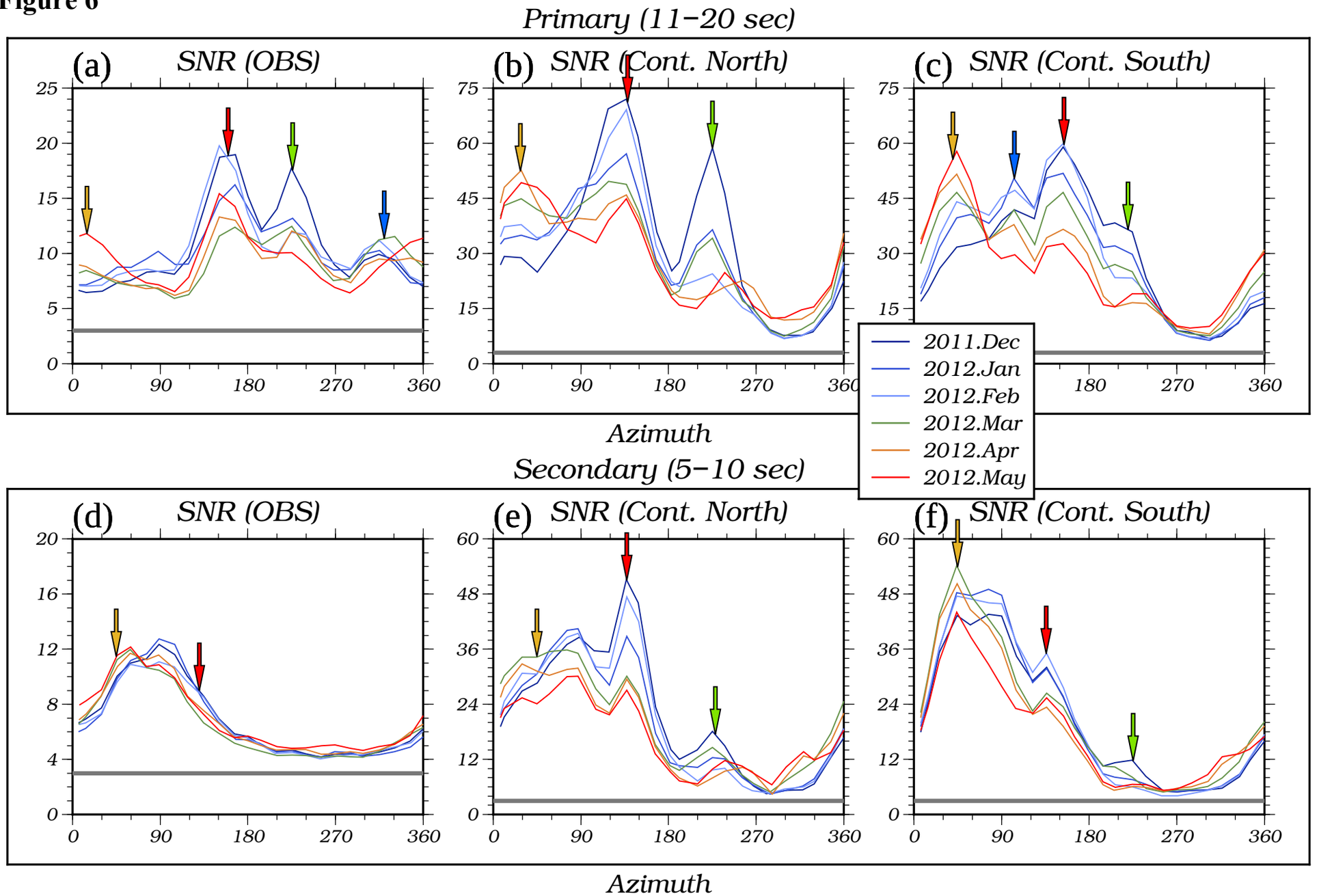

Figure 6. Monthly azimuthal variation of SNR summarizing results in Figs. 4 and 5 across the OBS stations (a,d), the continental stations north of 44°N (b,e), and the continental stations to the south (c,f). Results in the primary microseism band (11-20 sec) are shown in the top row and the secondary microseism band (5-10 sec) in the bottom row. The SNRs measured for each month are plotted with different colors where cooler colors indicate winter months and warmer colors indicate spring months. Azimuth is defined clockwise from north so that 0° means propagation to the north, 90° is propagation to the east, and so on. Note that vertical scales differ because SNR is higher for continental than oceanic stations and in the primary microseism than in the secondary microseism bands. For each period band, the primary peaks observed in each of the three diagrams are marked with color-coded arrows where the same color across the diagrams may be due to the same noise source.

Figure 7

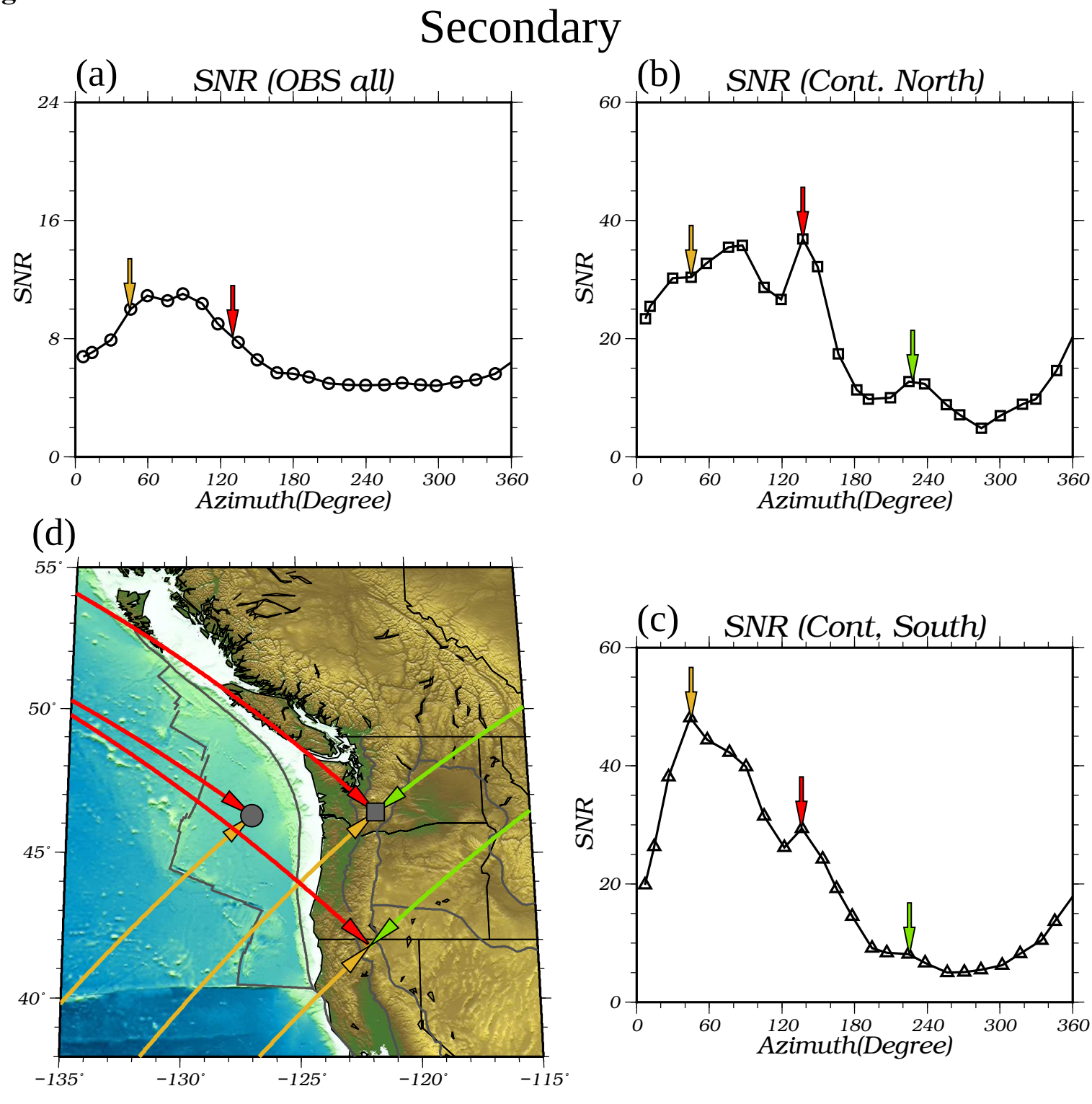

Figure 7. The azimuthal variations of SNRs averaged across all months for the secondary microseisms are shown in (a) for OBS stations, (b) for continental stations to the north of 44°N, and (c) for continental stations to the south. The same primary SNR peaks as marked in Fig. 6d-f are marked with arrows in three different colors. The back-projected

Figure 8

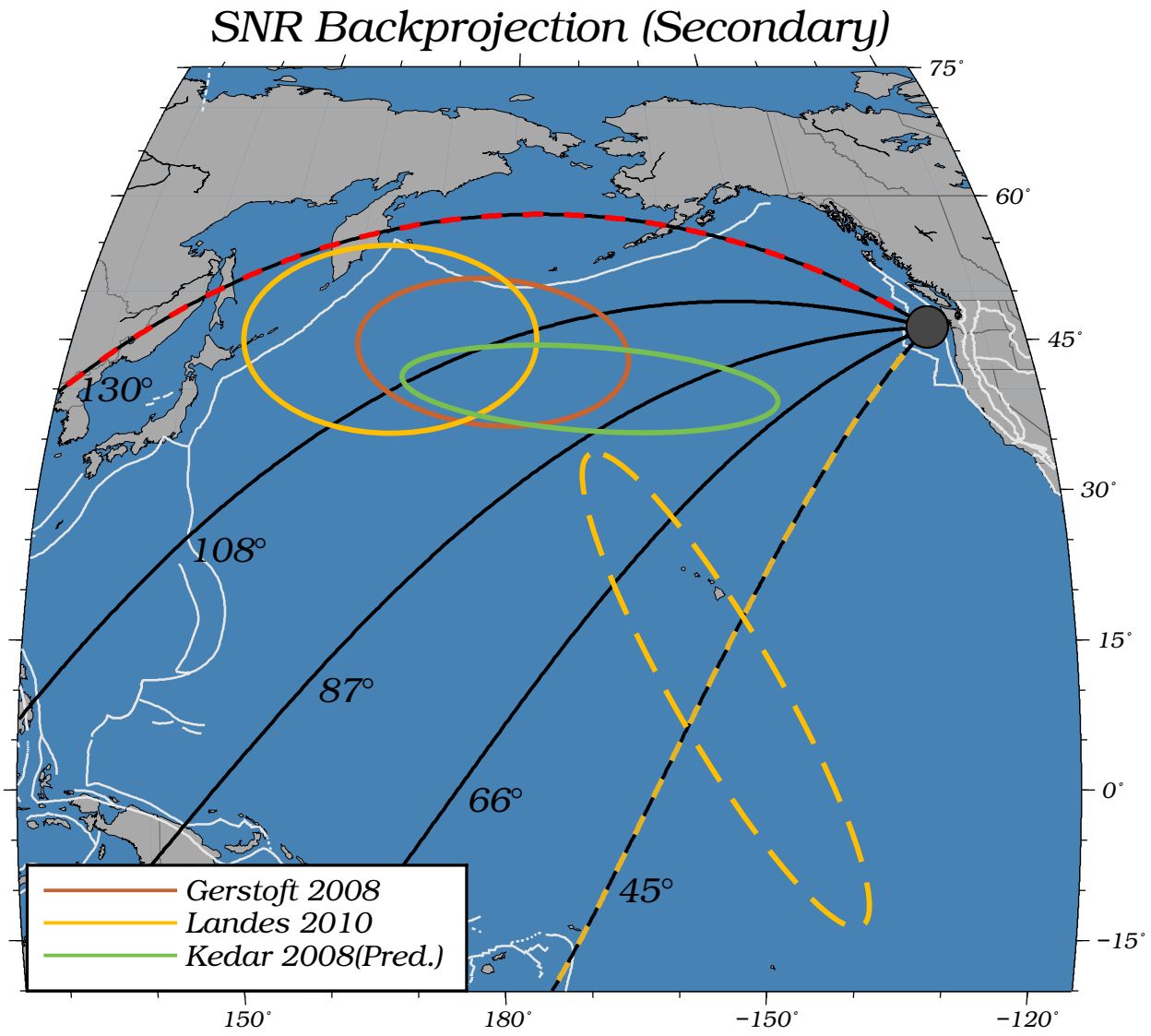

Figure 8. Possible source regions for the secondary microseisms. Great-circle lines are plotted at azimuths of 45° (yellow dash), 66°, 87°, 108° and 130° (red dash). Yellow and red dashed lines correspond exactly to the yellow and red arrows in Figs. 6 and 7. Orange and yellow solid ellipses indicate the source regions inferred by Gerstoft et al. (2008) and Landès et al. (2010) for body waves in ambient noise. The yellow dashed ellipse indicates a weaker source region from Landès. The green ellipse indicates the intense region of wave-wave interaction predicted theoretically by Kedar et al. (2008). (The source regions marked here are approximate.)

Figure 9

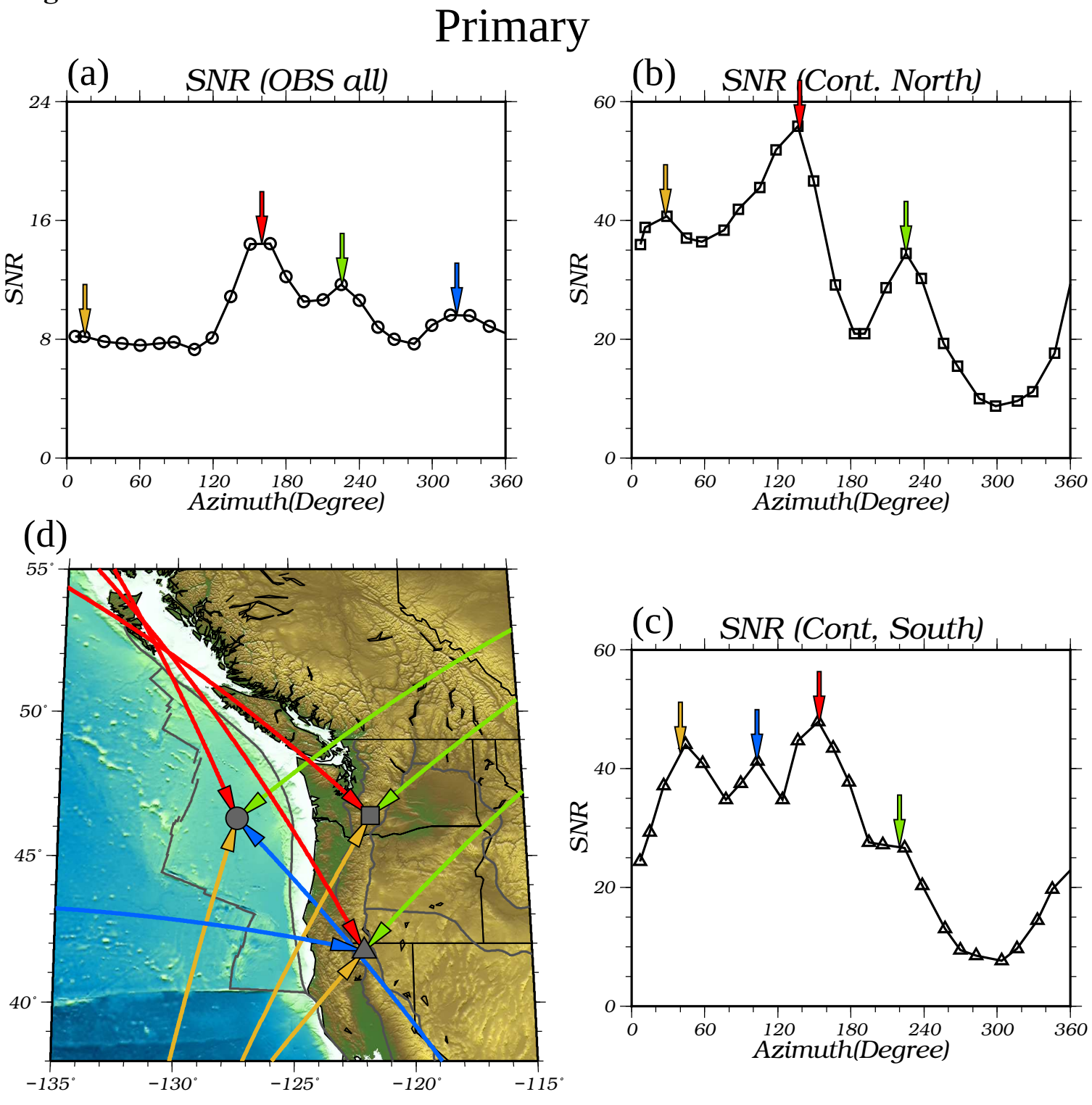

Figure 9. Similar to Fig. 7, but for the primary microseism.

Figure 10

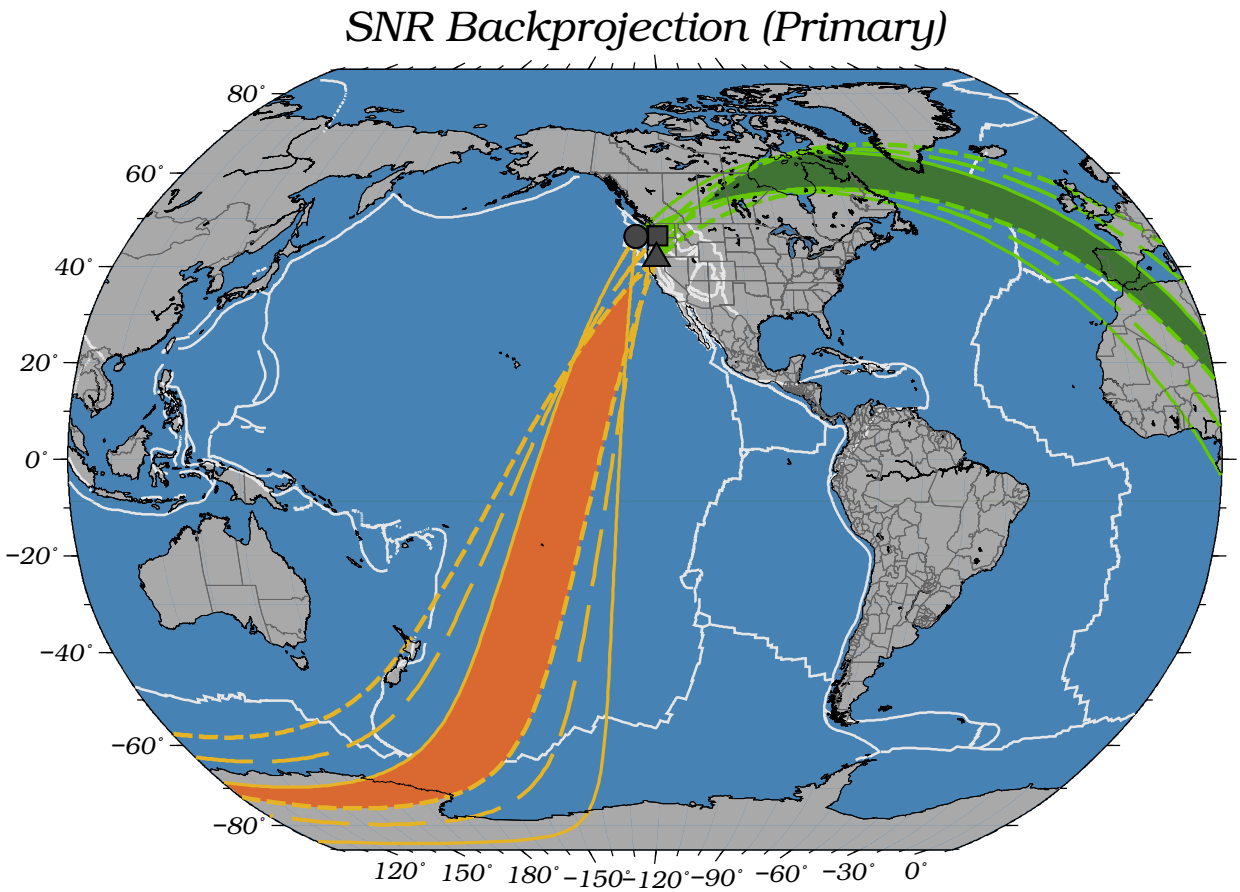

Figure 10. Possible source regions for the higher amplitudes near the green and yellow arrows shown in Figs. 6 and 9. The azimuth ranges of the SNR peaks are shown, respectively, with solid lines for OBS stations, long dashed lines for continental stations in the north, and short dashed lines for continental stations in the south. The azimuth ranges for the green arrows are chosen to be 218°-234° on the OBSs, 217°-233° on the northern continental stations, and 212°-228° on the southern continental stations. The azimuth ranges for the yellow arrows are chosen to be 5°-30° on the OBSs, 15°-40° on the northern continental stations, and 20°-45° on the southern continental stations. The peak near the yellow arrows is wider in azimuth as shown in Fig 6a,b,c and 9, thus the choices of wider ranges. The overlapping regions are colored dark green and orange for the green and yellow

Figure 11

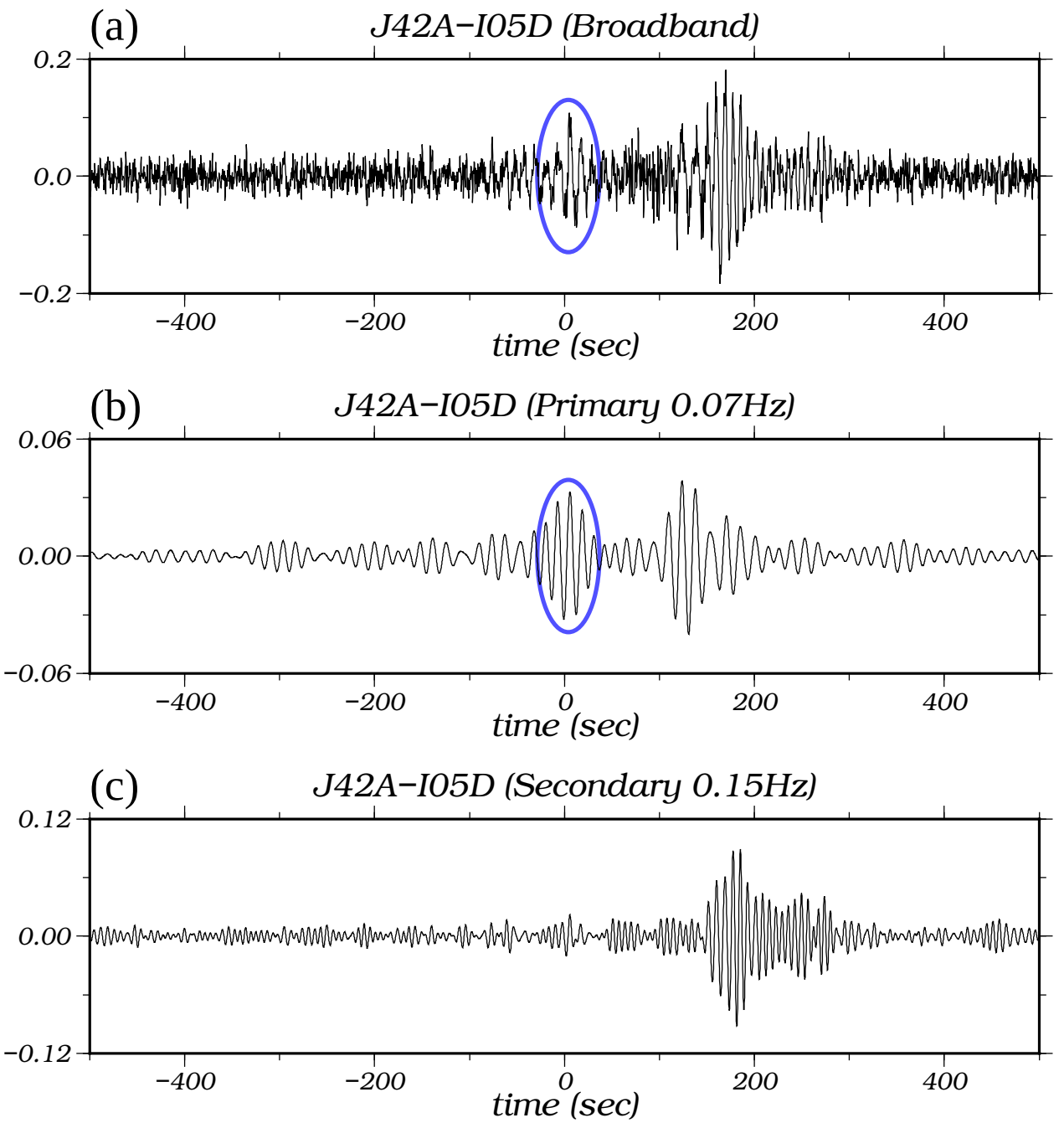

Figure 11. Example of precursory signals observed on ambient noise cross-correlations for station pair J42A-I05D. (a) Broadband cross-correlation. (b) Cross-correlation filtered in the primary microseism band. (c) Cross-correlation filtered in the secondary microseism band. The precursory signal window is marked with a blue ellipse in each diagram and is associated with the blue source region of Fig 12a.

Figure 12

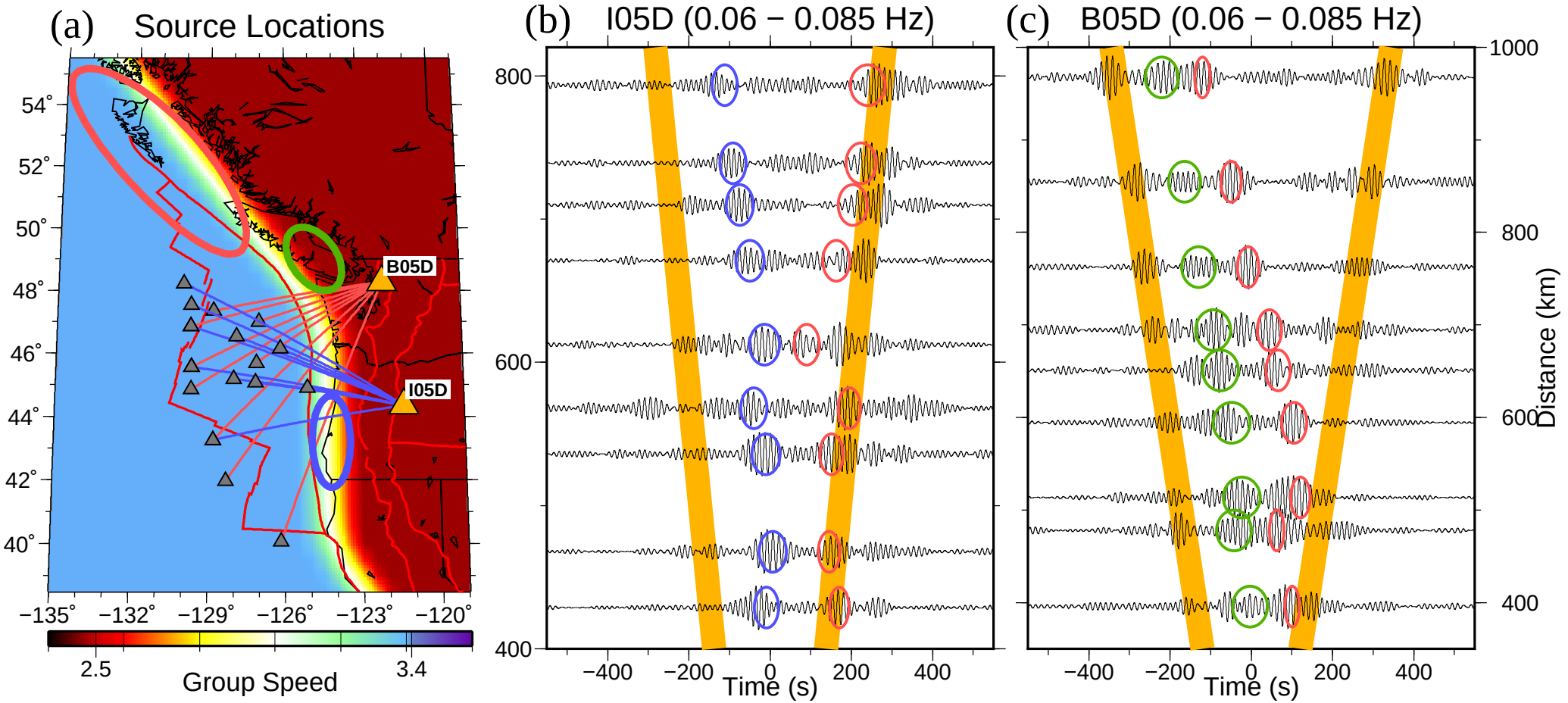

Figure 12. (a) The locations of the three potential local source regions are indicated with red, green, and blue ellipses. Background color shows the group speed model used in predicting the precursory signals produced by these sources. The two center stations B05D and I05D are marked with orange triangles. Paths between station pairs that are shown in (b) and (c) are indicated with blue and red lines, respectively. (b) The record section of example cross-correlations between the center station I05D and 9 OBSs. Blue ellipses indicate the predicted precursory arrival times from the blue potential source location shown in (a). Yellow lines indicate the predicted fundamental mode Rayleigh wave arrival times with a group speed of 3 km/sec. (c) Similar to (b), cross-correlations centered on stations B05D are shown. Red and green ellipses are associated with the red and green potential source locations identified in (a).

Figure 13

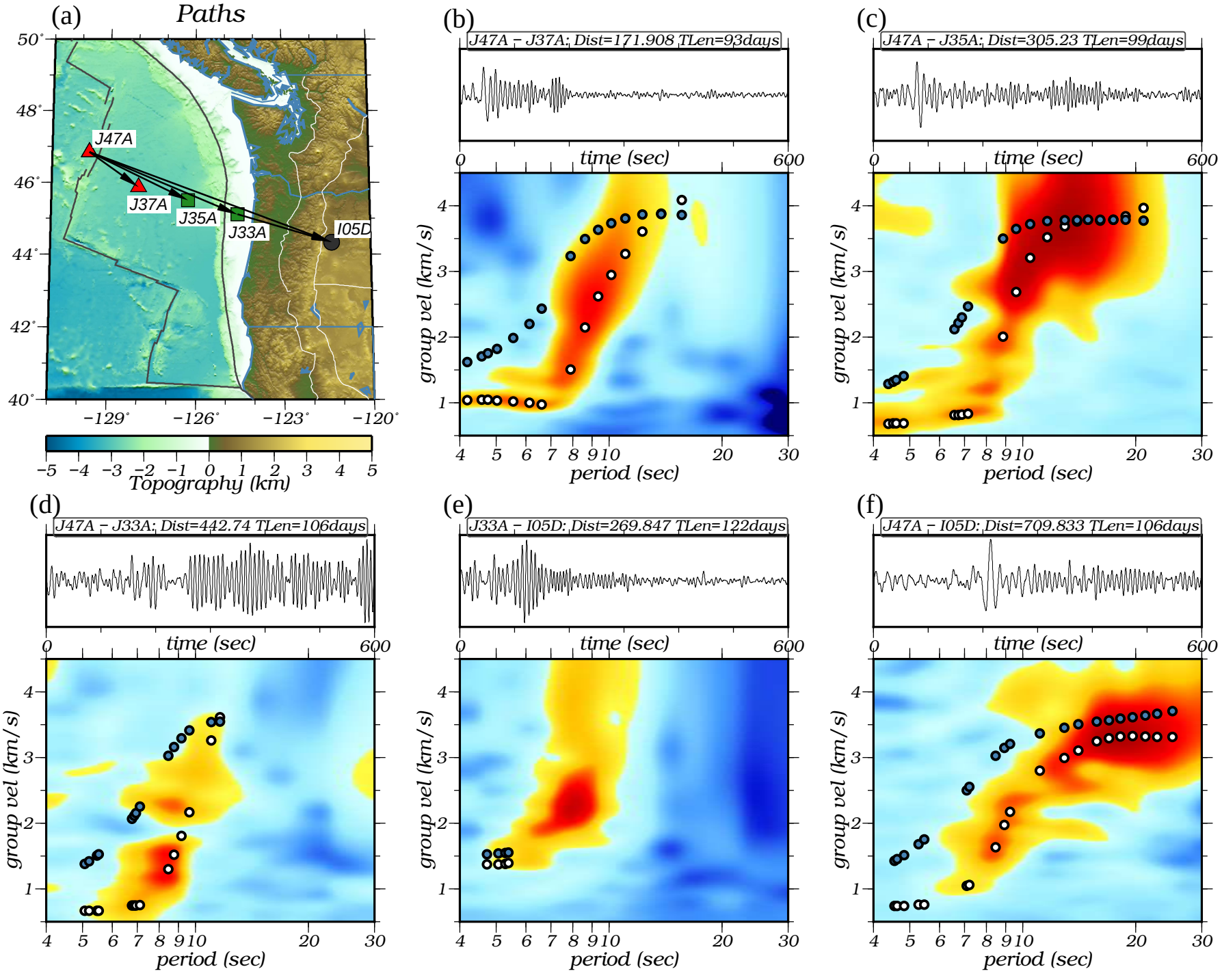

Figure 13. FTAN diagrams for five example paths showing surface waves propagating from the oceanic lithosphere onto the continent. (a) Locations of the paths are plotted with black arrows. The positive lag cross correlations and their corresponding FTAN diagrams are plotted in (b) - (f) for paths J47A-J37A, J47A-J35A, J47A-J33A, J33A-I05D, and J47A-I05D, respectively. The measured group and phase speed dispersion curves are shown with white and blue dots, respectively.